Lithos 265 (2016) 237–243

Contents lists available at ScienceDirect

Lithos

journal homepage: www.elsevier.com/locate/lithos

Evidence for H_2O-bearing fluids in the lower mantle from diamond inclusion

M. Palot [a,*], S.D. Jacobsen [b], J.P. Townsend [b], F. Nestola [c], K. Marquardt [d], N. Miyajima [d], J.W. Harris [e], T. Stachel [a], C.A. McCammon [d], D.G. Pearson [a]

[a] Department of Earth and Atmospheric Sciences, 1-26 Earth Science Building, University of Alberta, Edmonton, Canada
[b] Department of Earth and Planetary Sciences, Northwestern University, Evanston, IL, USA
[c] Dipartimento di Geoscienze, Università di Padova, 35131 Padua, Italy
[d] Bayerisches Geoinstitut, Universität Bayreuth, Bayreuth, Germany
[e] School of Geographical and Earth Sciences, University of Glasgow, Glasgow, United Kingdom

ARTICLE INFO

Article history:
Received 8 May 2016
Accepted 22 June 2016
Available online 30 June 2016

Keywords:
Diamond
Lower mantle
Deep water cycle
Brucite
Magnesioferrite
Ferropericlase
Dehydration melting

ABSTRACT

In this study, we report the first direct evidence for water-bearing fluids in the uppermost lower mantle from natural ferropericlase crystal contained within a diamond from São Luíz, Brazil. The ferropericlase exhibits exsolution of magnesioferrite, which places the origin of this assemblage in the uppermost part of the lower mantle. The presence of brucite–$Mg(OH)_2$ precipitates in the ferropericlase crystal reflects the later-stage quenching of H_2O-bearing fluid likely in the transition zone, which has been trapped during the inclusion process in the lower mantle. Dehydration melting may be one of the key processes involved in transporting water across the boundary between the upper and lower mantle.

1. Introduction

Earth's deep water cycle plays a critical role in the long-term geochemical evolution of our planet (Bercovici and Karato, 2003; Clog et al., 2013; Hirschmann, 2006; Ohtani et al., 2004,). Recent developments from high-pressure experiments and regional seismic studies (Emry et al., 2015; Schmandt et al., 2014), geochemical evidence from magmas (Wang et al., 2015), and the discovery of a natural hydrous ringwoodite (Pearson et al., 2014) affirm early theoretical predictions (Smyth, 1987) that the components of water can persist in minerals and melts as deep as the mantle transition zone (410–660 km depth). However, the water storage capacity of the dominant lower-mantle mineral assemblage, bridgmanite–$(Mg,Fe)(Si,Al)O_3$ (~75% vol.), Ca–Si perovskite (~5% vol.), and ferropericlase–(Mg,Fe)O (~20% vol.), is 10–15 times lower than in the transition zone (Bolfan-Casanova et al., 2002, 2003; Hernandez et al., 2013; Inoue et al., 2010; Joachim et al., 2013; Nestola and Smyth, 2015; Panero et al., 2015). Contrast in H_2O storage capacity between the transition zone and lower mantle could produce volatile-rich magmas by dehydration melting below 660 km depth (Hirschmann, 2006; Ohtani et al., 2004; Schmandt et al., 2014), potentially acting as a factory for diamond formation (Rohrbach and Schmidt, 2011; Thomson et al., 2016).

Owing to the scarcity of natural samples, direct evidence for the presence of H_2O in the Earth's lower mantle has been lacking. Mineral inclusions within diamonds provide the only natural samples from the Earth's lower mantle, and ferropericlase represents the most common inclusion in ultra-deep diamonds (Harte and Harris, 1994; Hutchinson et al., 1999; Kaminsky et al., 2001; Palot et al., 2012; Stachel et al., 2002). To search for evidence for the presence of H_2O below 660 km within the lower mantle, we conducted a coupled spectroscopic and microscopic study of a large natural ferropericlase inclusion and its host diamond, from the São Luíz river, Juina, Brazil.

1.1. Sample description and analytical techniques

The ferropericlase inclusion, exposed by cracking the diamond, consists of two pieces, GP3a, a ~300 μm fragment of a larger (~450 μm) crystal, and GP3b which remains in the diamond. The host diamond exhibits the highly irregular morphology typical of ultra-deep diamonds and is mostly colorless (Fig. 1).

Micro-FTIR analyses were conducted using a Thermo-Nicolet Nexus 470 Fourier-transform infrared spectrometer fitted with a continuum

* Corresponding author at: Laboratoire Magmas et Volcans, Université Jean Monnet, Saint-Etienne, France.
E-mail address: mederic.palot@gmail.com (M. Palot).

http://dx.doi.org/10.1016/j.lithos.2016.06.023
0024-4937/

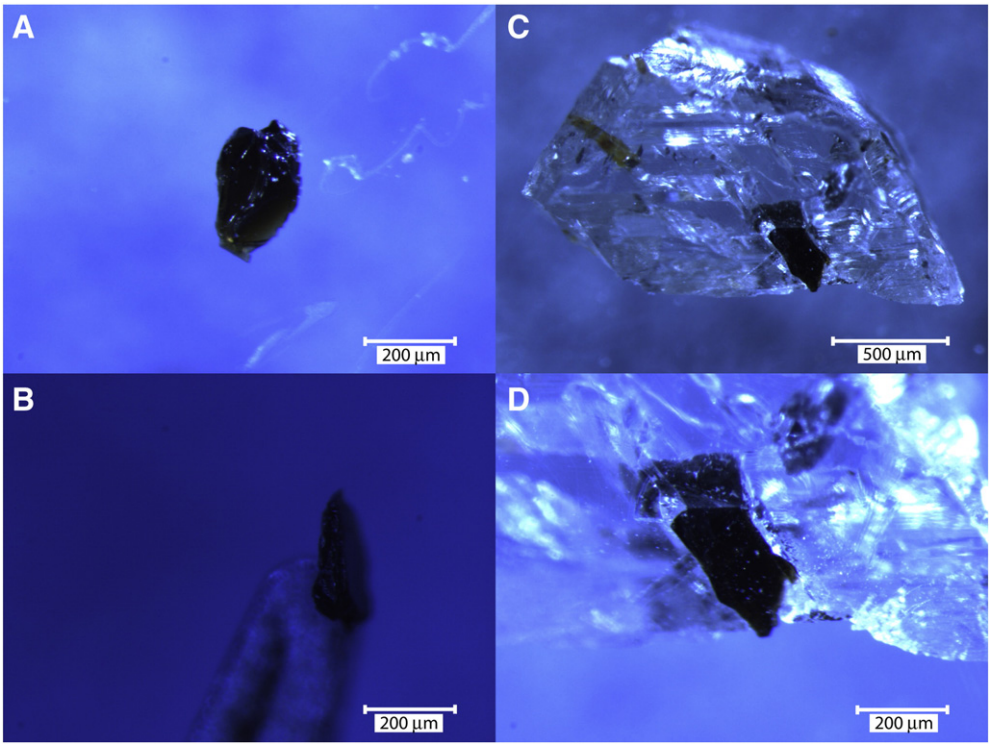

Fig. 1. Images of the ferropericlase crystals GP3a and GP3b and the host diamond. A) GP3a is a ~300 µm fragment of a larger (~450 µm) inclusion. B) Side view of GP3a crystal. C) GP3b is the remaining fragment of the fPer inclusion in the diamond. The host diamond is colorless, exhibits an irregular morphology, and shows evidence of plastic deformation. D) Enlarged view of the area of the fPer inclusion.

infrared microscope with a KBr beam splitter at the DeBeers Laboratory of Diamond Research at the University of Alberta, Canada. The system was continuously purged with a dry nitrogen–oxygen mix. IR-Spectra (4000–600 cm^{-1}) were acquired in transmitted mode using an aperture size of 100 µm; for each analysis, 200 scans were collected with a resolution of 4 cm^{-1}. Typical detection limits for the presence of nitrogen in diamond and hydrogen-related defects in minerals are better than 10 at.ppm.

Synchrotron–FTIR analyses were conducted at the National Synchrotron Light Source, beamline U2A, Brookhaven National Laboratory, USA. Measurements were made with a Bruker Vertex 80/v FTIR and Hyperion 2000 IR microscope set to 1024 scans. The spatial resolution of ~10 × 10 µm was set using a knife-edge aperture and the sample ranged in thickness from approximately 50–100 µm at the measurement points shown in Fig. 2A.

Single-crystal X-ray diffraction measurements were performed by a new prototype Rigaku–Oxford Diffraction Supernova single-crystal X-ray diffractometer (kappa geometry), equipped with a PILATUS 200K (Dectris) area detector at the Dipartimento di Geoscienze, Università di Padova, Italy. This diffractometer is equipped with a X-ray micro-source (MoKα wavelength), a spot size of ~120 µm and is characterized by a brightness at least 10 times higher than a conventional X-ray source. The sample-to-detector distance was 68 mm and the X-ray source worked at 50 kV and 0.8 mA. The Pilatus detector ensures extremely high sensitivity and practically no noise.

Confocal Raman spectroscopy measurements were carried out at Northwestern University, USA, using a custom-built Olympus BX microscope, 100× objective, Melles-Griot 458 nm laser, and Andor Shamrock 303-i spectrometer. Laser power at the sample was less than 1 mW to avoid damage. Spectra were collected for 5 min each and the measurement spot size was less than 5 µm diameter.

Electron transparent foils were prepared using a FEI Scios FIB device allowing to switch between electron and ion beam. Foil dimensions are 20 × 8 $µm^2$ with a thickness of about 100 nm. The foil was recovered using the in situ easy-lift system. Transmission electron microscopic (TEM) investigations were performed with a FEI Titan 80–200

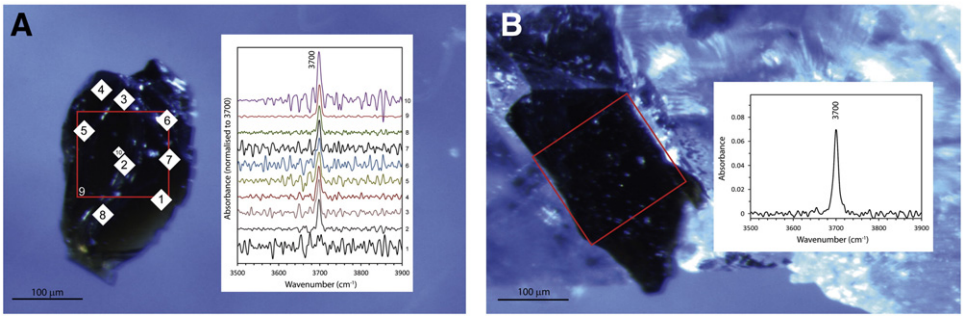

Fig. 2. Spatial distribution of synchrotron-FTIR spectra in ferropericlase inclusion GP3a within São Luíz diamond. Squares represent the size of each spot analysis. Sharp absorption bands at ~3700 cm^{-1} are observed in both fragments, which correspond to sparsely distributed, nano-scale brucite precipitates. A) Spectra of the loose fragment GP3a of ferropericlase between 3500 and 3900 cm^{-1}. Spectra were baseline corrected. B) Spectrum of ferropericlase fragment GP3b, still embedded in the diamond. Spectrum was corrected for both the response of the host diamond and the baseline.

microscope at Bayerisches Geoinstitut, University of Bayreuth, Germany, using conventional TEM, high-resolution (HR)-TEM, as well as scanning (S)-TEM modes. The microscope was operated at an acceleration voltage of 200 kV with an electron beam generated by an extreme brightness field emission gun (X-FEG) Schottky electron source. The TEM is equipped with a post-column Gatan imaging filter (GIF Quantum®SE). In STEM mode, the high-angle annular dark field (HAADF) detector and/or the bright or dark field (BF/DF) detectors were used to acquire the signal. For energy dispersive X-ray (EDX) measurements, we used the windowless SuperX-EDS detector with 4 SDD in scanning mode and obtained high peak to background EDS analyses at low beam currents over more than 4 h acquisition.

For Mössbauer spectroscopy, inclusions were mounted on plastic foils and placed behind a hole with diameter 300 μm (GP3a) or 500 μm (GP3b) drilled into Ta foil with 25 μm thickness. The dimensionless thickness of the samples is roughly 5 (corresponds to 10 mg Fe/cm^2) based on the estimated physical thickness and composition. Mössbauer spectra were recorded at room temperature (293 K) in transmission mode on a constant acceleration Mössbauer spectrometer with a nominal 370 MBq ^{57}Co high specific activity source in a 12 μm thick Rh matrix at Bayerisches Geoinstitut, University of Bayreuth, Germany. The velocity scale was calibrated relative to 25 μm thick α-Fe foil using the positions certified for (former) National Bureau of Standards standard reference material no. 1541; line widths of 0.36 mm/s for the outer lines of α-Fe were obtained at room temperature. Measurement times for each spectrum varied from 4 to 5 days. Spectra were fit using the program MossA (Prescher et al., 2012).

2. Results

2.1. Scanning electron and transmission electron microscopy, energy dispersive X-ray, and Raman and Mössbauer spectroscopy

The surface of GP3a exhibits "tie"-like features (see supplementary Fig. S1) produced by magnesioferrite crystals ~1 μm in length that have precipitated along dislocations near the ferropericlase surface and as ~10–20 nm isolated octahedra within the bulk ferropericlase (Fig. 3). The EDX-spectra reveal a magnesioferrite composition of approximately $Mg(Fe_{0.75}Cr_{0.17}Al_{0.08})_2O_4$ (Fig. 3). Raman mapping of the ferropericlase inclusion reveals a prominent band at 600 cm^{-1}, also characteristic of magnesioferrite (see supplementary Fig. S2). Mössbauer spectroscopy analysis of GP3a and GP3b shows little or no Fe^{3+} ($Fe^{3+}/\Sigma Fe = 0.01 \pm 0.01$ and 0.02 ± 0.02, respectively, see supplementary Fig. S3).

2.2. Single-crystal X-ray diffraction

X-ray diffraction data for GP3a confirm the identification of magnesioferrite with the presence of the two main diffraction peaks with *d*-spacings of 2.51 and 2.97 Å (Fig. 4). Although ferropericlase and magnesioferrite can show a certain degree of diffraction peak overlap, this is not the case for the two peaks of magnesioferrite measured in GP3a, allowing its definitive identification. The lattice parameter of the magnesioferrite was found to be $a = 8.382(8)$ Å, with fitted unit-cell volume $V = 589.0(9)$ Å^3, which is consistent with the cell volume predicted for the magnesioferrite composition measured by EDX ($V = 585.13$ Å^3). In order to produce pseudo-single-crystal X-ray diffraction spots like those shown in Fig. 4, there must be a high density of nanometer-sized magnesioferrite grains in topotaxial relation to the ferropericlase, which was confirmed by TEM (supplementary Fig. S4).

2.3. Infrared spectroscopy

Nitrogen content in the host diamond is below the detection limit of Fourier-transform infrared spectroscopy (micro-FTIR), a common characteristic of ultra-deep diamonds (Hutchinson et al., 1999; Kaminsky et al., 2001; Palot et al., 2012; Stachel et al., 2002). The host diamond displays also no hydrogen-related absorption band at 3107 cm^{-1}, attributed to nitrogen and hydrogen in the form of a VN_3H defect (Goss et al., 2014), which is consistent with the absence of detectable nitrogen. Other absorption bands typically associated with hydrogen in diamond are also not observed (supplementary Fig. S5).

Micro-FTIR detected a sharp absorption band at 3697 cm^{-1} within diamond inclusions GP3a and GP3b, associated with brucite–($Mg(OH)_2$) precipitates within both fragments of the ferropericlase. This absorption band is attributed to hydrous phase of brucite in the ferropericlase inclusion rather than structurally bond OH defects in agreement with experimental studies (e.g. Bolfan-Casanova et al., 2002; Joachim et al., 2013). Synchrotron–FTIR mapping reveals a fairly homogeneous spatial distribution of the 3700 cm^{-1} peak throughout both ferropericlase crystals (Fig. 2). In contrast to FTIR, X-ray diffraction, scanning electron microscopy (SEM), and Raman spectroscopy did not detect brucite in GP3 (see supplementary material), indicating that the brucite occurs as sparsely distributed, nano-scale precipitates (Joachim et al., 2013). Structurally

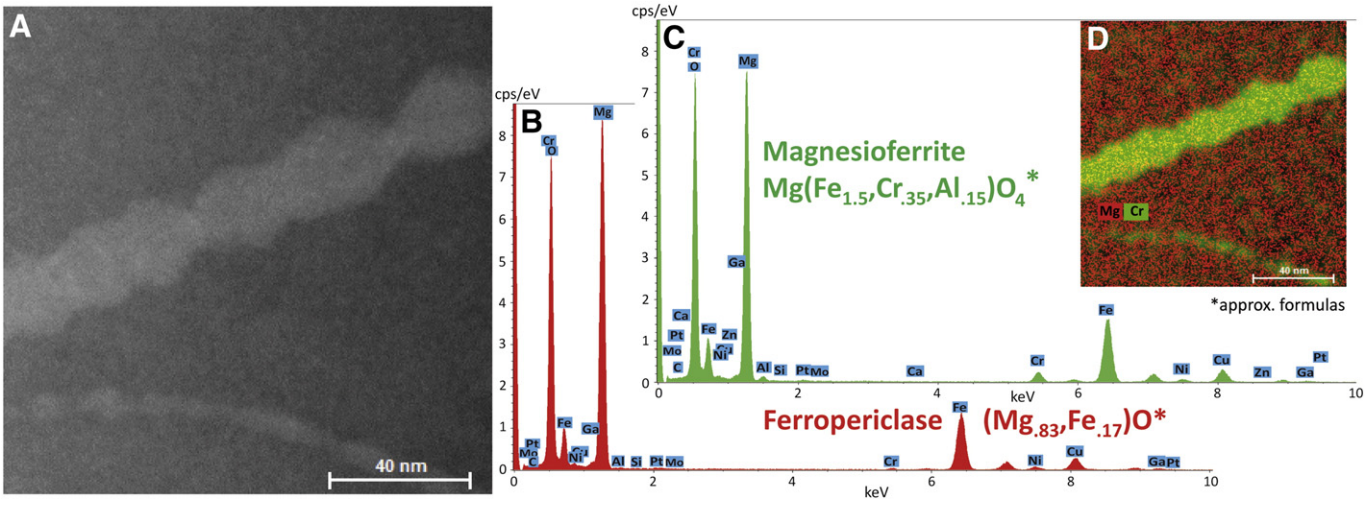

Fig. 3. A) STEM image using Z-contrast conditions. The magnesioferrite is linearly aligned along a pre-existing dislocation. B) EDX-spectrum of the ferropericlase matrix with the approximate composition indicated (within 10%). C) EDX-spectrum of the exsolved magnesioferrite (spinel structure) with the approximate composition indicated (within 10%). D) EDX-map highlighting the regional distribution of elevated Cr-content (green) with the complementary distribution of Mg (red).

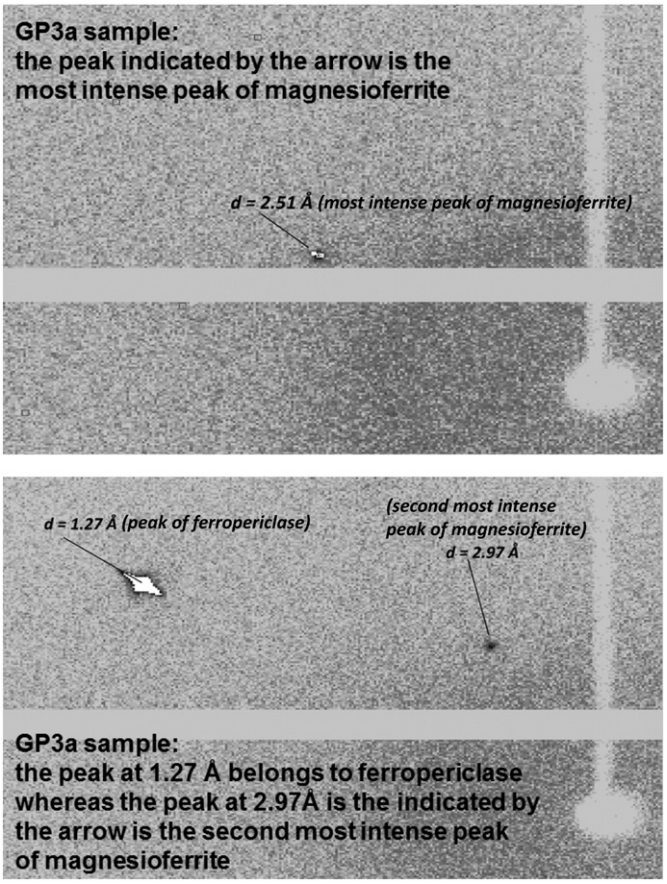

Fig. 4. Single-crystal X-ray diffraction images of GP3a crystal showing the main diffraction peaks of magnesioferrite and ferropericlase. The images show the two main diffraction peaks of magnesioferrite having a d-spacing of 2.51 and 2.97 Å, in their exact order of expected relative intensity. The peak at 1.27 Å belongs to ferropericlase.

bound OH bands at 3320 and 3480 cm^{-1} are below detection limits of FTIR. We estimate the bulk H_2O content of GP3a to be ~30 ± 4 ppm (2σ) by integrating the IR absorption band at 3700 cm^{-1} and using the Beer–Lambert law:

$$A_i tot = \varepsilon_i.C.t$$

where $A_i tot$ is the integrated absorbance (A_i) multiplied by three (Libowitzky and Rossman, 1996), ε_i is the extinction coefficient in $l.(mol.H_2O)^{-1}.cm^{-2}$, C is the concentration in mol $H_2O.l^{-1}$, and t is the sample thickness. The concentration of water in ppm is

$$C(\text{ppm } H_2O) = (3\ A_i tot/\varepsilon_i/t) \times 1000 \times 18/\rho$$

where $A_i tot$ is estimated to be 0.1838, 0.1902, and 0.2815; $t = 60.10^{-4}$ cm; 18 represents the molar weight of H_2O; and ρ is the density of ferropericlase (taken as 4.2 $g.cm^{-3}$), ε_i = 14,056 $l.(mol.H_2O)^{-1}.cm^{-2}$ using the calibration of Libowitzky and Rossman (1997):

$$\varepsilon_i = 246.6 \times \left(3753\text{–mean wave number of the OH stretching in}cm^{-1}\right)$$

Calculations yield water concentration of 28 ppm for spectrum 1, 42 ppm for spectrum 2, and 27 ppm for spectrum 3. We considered an uncertainty of ± 10 μm in the determination of the overall sample thickness and an uncertainty of 1% in determining the area below the relevant band.

3. Discussion

3.1. Evidence for a lower-mantle origin of the studied diamond

It is important to unambiguously establish the lower-mantle origin of the studied sample, as some ferropericlase inclusions in diamonds may originate in the transition zone and the upper mantle (Brey et al., 2004). Relatively Fe-rich "intermediate" ferropericlase compositions are likely to have been produced by reaction between carbonate melt and peridotite in the transition zone (Rohrbach and Schmidt, 2011; Thomson et al., 2016). The GP3 ferropericlase composition is among the most Mg-rich recorded from Juina, with an Mg number (Mg/(Mg + Fe) of 84 ± 8 (Figs. 3 and S6). In addition to the highly irregular morphology and very low nitrogen content of the host diamond, the nano-scale textures and the very low Fe^{3+} content of the included ferropericlase provide strong supporting evidence of a lower-mantle origin.

Specifically, the isolated precipitates of magnesioferrite, visible as octahedra, form a topotaxial growth relationship with ferropericlase (supplementary Fig. S4). The even distribution of euhedral octahedral spinel in the ferropericlase matrix indicates that magnesioferrite precipitated directly from ferropericlase. The observation of magnesioferrite exsolution, dispersed at a fine scale through the ferropericlase, is consistent with both experimental (Frost et al., 2010) and natural observations (Kaminsky et al., 2014; Wirth et al., 2014) that associate this process with retrogression from P–T conditions in the uppermost lower mantle. Fig. 5 illustrates the formation mechanism of the magnesioferrite exsolution. Diamond initially trapped Fe^{3+}-, Al^{3+}-, and Cr^{3+}-bearing ferropericlase as an inclusion in the lower mantle (see supplementary Fig. S6 for initial bulk composition of the ferropericlase). During exhumation, stress accumulates at the interface between diamond and ferropericlase due to differing thermal expansion coefficients and compressibility, forming dislocations. This phenomenon is enhanced by plastic deformation of the diamond (observed as striae at the diamond surface), transmitting stress to the ferropericlase. Such dislocations serve as nucleation sites for magnesioferrite near the surface, indicating that magnesioferrite precipitated following inclusion in the diamond.

In order to provide constraints on the phase relationships between ferropericlase and magnesioferrite, we made a phase diagram in the system $MgO–Fe_2O_3–M^{3+}{}_2O_3$ (Fig. 5), which is adapted from available data (i.e. phase transition at ambient pressure with additional high pressure data from McCammon et al., 1998). In order to estimate the temperature of the ferropericlase − > ferropericlase + magnesioferrite exsolution phase boundary at high pressure, we evaluated the thermoelastic parameters of the magnesioferrite phase from P-V-T data published by Levy et al. (2004). Using EosFit7c to fit the equations of state (Angel et al., 2014; Gonzalez-Platas et al., 2016), we obtain K_{T0} = 181.5 GPa for the bulk modulus and $K_0' = 6.32$ for the first pressure derivative. Thermal expansion coefficients, $\alpha_0 = 3.2 \times 10^{-5}\ K^{-1}$ and $\alpha_1 = 1.004 \times 10^{-8}\ K^{-1}$, were obtained following the formulation of Berman (1998). For the temperature dependence of the bulk modulus, we used $dK_{T0}/dT = -0.020$ GPa/°C, typical of minerals displaying order–disorder processes. For ferropericlase, we used equation of state parameters of high-spin fp (<40 GPa) with 15 mol% Fe. Based on the volume difference between fp and magnesioferrite, we estimate that the exsolution boundary could shift to higher temperature by up to 150 °C per GPa, placing the likely exsolution temperature at > 1600 °C near the top of the lower mantle (Fig. 5). The high-pressure polymorph of magnesioferrite (formed above 25 GPa) is apparently unable to re-dissolve into ferropericlase (Wirth et al., 2014). Thus, the reaction responsible for the redistribution of M^{3+} (Al^{3+}, Fe^{3+}, Cr^{3+}) from ferropericlase to magnesioferrite $(Mg, Fe^{2+})(M^{3+})_2O_4$ should take place at higher temperatures compared to the present phase diagram, which could place our sample at even greater depth. We interpret the observation of different dislocation features with varying thicknesses of magnesioferrite precipitates (Fig. 3), where younger dislocations had less time to grow

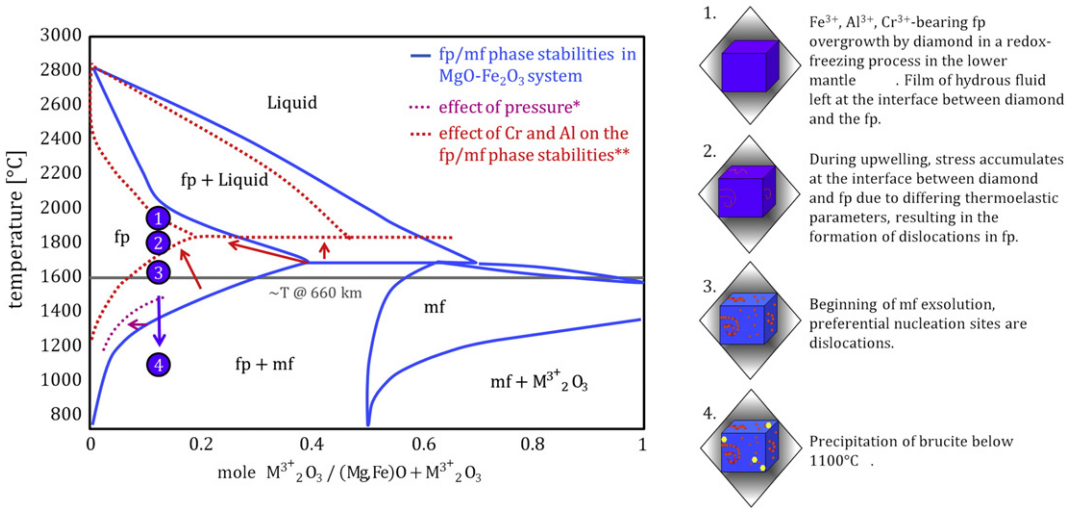

Fig. 5. Left—Schematic phase relationships for ferropericlase (fp) and magnesioferrite (mf) with decreasing temperature. This diagram is adapted from the phase diagram available at http://www.crct.polymtl.ca/fact/documentation/. *The fp phase stability decreases relative to ambient pressure as indicated by the purple dotted lines, which are both heuristic estimates based on ambient pressure phase diagrams and experiments at 18 GPa (McCammon et al., 1998). This relative shift is for pure Mg–Fe system. **Incorporation of Cr and Al in the system tends to shift the phase stability fields toward higher temperatures (red dotted lines). M^{3+} for trivalent cations. Overall increased pressure and addition of trivalent cations increase the temperature of magnesioferrite exsolution (see Fig. S7). Right—Schematic history of the formation mechanisms of the ferropericlase–magnesioferrite–brucite assemblage.

magnesioferrite, as an index for continuous exsolution during upwelling from lower-mantle depths, where new dislocations formed. The Mössbauer observation is consistent with stabilization of Fe^{3+} in high-pressure magnesioferrite instead of ferropericlase at lower-mantle conditions (McCammon et al., 1998).

3.2. Evidence for H_2O-bearing fluid trapped in the diamond within the lower mantle

The presence of brucite in the ferropericlase reflects the interaction of H_2O-bearing fluid trapped in the diamond. Our observation of the 3700 cm^{-1} band is consistent with high P-T hydrothermal experiments on MgO that attribute brucite precipitates to diffusion of molecular water near the surface of periclase at temperatures >1200 °C, which reacts with the host oxide crystal during cooling (Joachim et al., 2013). The observation of brucite by FTIR, but not with Raman, X-ray, TEM, and SEM in the TEM foils, illustrates that brucite is likely present as isolated nano-precipitates (Joachim et al., 2013) and thus indicating H_2O diffusion at high P-T. Alternatively, ferropericlase may have incorporated few 10 s ppm of water which later exsolved out to form trace amounts of brucite. Following this way, there is, however, no simple explanation for the absence of structurally bound OH bands at 3320 and 3480 cm^{-1} in the ferropericlase. In both cases, H_2O-bearing fluid would have been trapped in the uppermost lower mantle during the formation of diamond and ferropericlase through redox-freezing process (Rohrbach and Schmidt, 2011; Thomson et al., 2016; Walter et al., 2011) (Fig. 6). The examination of several FIB foils did not show nano-precipitates of brucite in micro cracks in the ferropericlase or at the ferropericlase–diamond interface, which indicates that encapsulation of the fluid at a later stage is very unlikely (i.e. in the transition zone/upper mantle). Brucite would precipitate during a later-stage quenching or slow cooling of this H_2O-bearing fluid, which would have formed at shallower depths likely in the upper mantle/transition zone. Diamond is acting as an inert capsule, fully isolated from the environment.

Evidence for brucite precipitates have also been observed in ferropericlase and ringwoodite crystals synthesized at 24 GPa and 1400 °C under hydrous conditions (Bolfan-Casanova et al., 2003) and after re-examination, it is a prominent feature of the IR spectrum in natural hydrous ringwoodite included in diamond (Pearson et al., 2014) clearly indicating high water activity during incorporation (Fig. 6A). Bridgmanite–ferropericlase mixtures synthesized from very hydrous ringwoodite at 30 GPa and 1600 °C also display a prominent brucite peak (Schmandt et al., 2014) (Fig. 6B). Ferropericlase containing 7 mol% FeO and $Fe^{3+}/\Sigma Fe = 0.03$, and annealed under water-saturated conditions at ~1200 °C and 20 GPa (Bolfan-Casanova et al., 2002), display bands at 3320, 3480, and 3700 cm^{-1} (Fig. 6C). Whereas the 3320 and 3480 cm^{-1} bands are attributed to structurally bound OH impurities, the 3700 cm^{-1} band in these experiments was interpreted as brucite (Bolfan-Casanova et al., 2002). Brucite begins to precipitate during quenching likely as a result of decreasing maximum solubility of protons in VOH^{-} centers with decreasing temperature, leading to a simultaneous decrease in the bands at about 3300 cm^{-1} (Joachim et al., 2013). Another possibility to explain the absence of structurally bound OH bands at 3320 and 3480 cm^{-1} is that the magnesioferrite had already sequestered trivalent cations from the ferropericlase during ascent and cooling below ~1000 °C (Fei and Mao, 1993), where brucite formed. However, experiments in Joachim et al. (2013) were performed in absence of any trivalent cations and OH defects were still visible in IR-spectra.

3.3. Implication for diamond formation and mantle geodynamic

Here we propose the most likely sequence of events recorded in the studied inclusion assemblage (Fig. 5): (1) an initially homogenous ferropericlase containing trivalent (Fe^{3+}, Cr^{3+}, Al^{3+}) grows in situ with diamond in a redox-freezing process (Rohrbach and Schmidt, 2011; Thomson et al., 2016; Walter et al., 2011) below the 660 km discontinuity in the uppermost lower mantle. Following formation of the diamond and ferropericlase, a thin film of H_2O-bearing fluid would have been left at the interface between the ferropericlase and diamond (e.g. Nimis et al., 2016) at very high temperatures (>1800 °C).) (2) On ascent and cooling, the different thermoelastic properties of diamond and ferropericlase led to the formation of dislocations in ferropericlase at its interface with diamond. (3) Upon cooling to below 1800 °C (Fig. 2), magnesioferrite precipitated along pre-existing dislocations and within the host ferropericlase. (4) During further cooling (but still at >1200 °C), water slowly diffused into the near-surface of the inclusion (Joachim et al., 2013). During further decompression, the water cannot

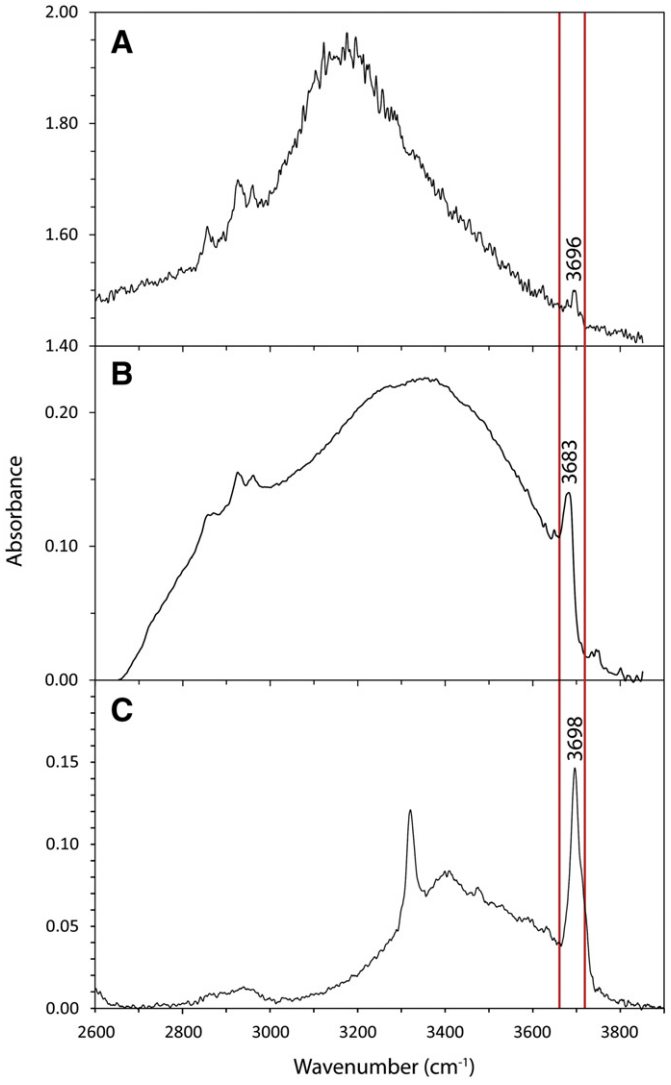

Fig. 6. A) Spectrum of hydrous ringwoodite inclusion in Juina diamond JUc29 (Pearson et al., 2014). The sharp absorption band indicative of brucite precipitate is observed at ~3696 cm^{-1}. Spectrum was corrected for both the response of the host diamond and the baseline. B) Spectrum of bridgmanite plus ferropericlase plus hydrous melt-quench mixture synthesized from hydrous ringwoodite (Schmandt et al., 2014) at 30 GPa and 1600 °C. C) Spectrum of ferropericlase annealed under water-saturated conditions at 20 GPa and 1200 °C and containing $Fe^{3+}/\Sigma Fe = 0.03$ (Bolfan-Casanova et al., 2002). Brucite precipitates are a common feature of minerals grown under hydrous conditions at conditions near and within the lower mantle.

be incorporated into the ferropericlase which leads to brucite precipitation at shallower depths.

Magnesioferrite exsolutions provide further evidence for a lower-mantle origin of ferropericlase, supporting the most evident lower-mantle source compared to exotic modes of formation in the upper mantle or transition zone. The OH now bound to brucite must have it origin in the uppermost lower mantle in the form of an H_2O-bearing fluid.

This hydrous fluid may represent the pro-grade dehydration breakdown of ringwoodite, with water and chromium from ringwoodite partitioning into the ferropericlase and then the magnesioferrite, during the downward motion of a subducted slab across the 660 km discontinuity. The observation of brucite in diamond in both ringwoodite (Pearson et al., 2014) and the studied ferropericlase inclusions indicates that their formation can occur under hydrous conditions in the transition zone as well as within the lower mantle. The contrast in storage capacity between transition zone and lower-mantle assemblages leads to excess water, which can promote dehydration melting below 660 km depth (Hirschmann, 2006; Ohtani et al., 2004; Schmandt et al., 2014). This process may generate volatile-rich melt at the top of the lower mantle and could act as a locus for diamond formation (Harte, 2010). Dehydration melting may be one of the key processes involved in transporting recycled slab-derived water across the boundary between the upper and lower mantle.

4. Conclusion

The observation of magnesioferrite precipitates in ferropericlase inclusion by SEM, TEM, EDX, Raman spectroscopy, and X-ray diffraction demonstrates that the studied diamond derived from the upper part of the lower mantle. The identification of brucite by infrared spectroscopy is best explained by the entrapment of H_2O-bearing fluid during diamond formation in the uppermost lower mantle. During further cooling, water slowly diffused into the near-surface of the inclusion leading to brucite precipitation at shallower depths likely in the transition zone or upper mantle.

Our data support the idea that dehydration melting generates volatile-rich fluids/melts at the top of the lower mantle, yet being a key process for diamond genesis and for transportation of water across the 660 km discontinuity.

Acknowledgments

We are very grateful to the editor, Geoff Bromiley, and an anonymous reviewer for their constructive and careful reviews that improved the strength and clarity of this manuscript. MP was supported by the Deep Carbon Observatory and a Canada Excellence Research Chair award to DGP. SDJ acknowledges support from the NSF (EAR-1452344), the Carnegie/DOE Alliance Center (CDAC), the David and Lucile Packard Foundation, and the Alexander von Humboldt Foundation. Portions of this work were performed at beamline U2A of the National Synchrotron Light Source (NSLS), Brookhaven National Laboratory. U2A is supported by COMPRES under NSF Cooperative Agreement EAR 11-57758 and DOE-NNSA (DE-FC-52-08NA28554, CDAC). Use of the NSLS was supported by the DOE-BES (DE-AC02-98CH10886). FN is supported by the ERC Starting Grant (no. 307322). The diamond used for this study was kindly donated by De Beers to JWH. We thank Zhenxian Liu for his help with the synchrotron–FTIR measurements and Sylvain Petitgirard for help with FIB sample preparation. The FIB facility at Bayerisches Geoinstitut is supported by DFG grant INST 91/315-1 FUGG.

Appendix A. Supplementary data

Supplementary data to this article can be found online at http://dx.doi.org/10.1016/j.lithos.2016.06.023.

References

Angel, R.J., Gonzalez-Platas, J., Alvaro, M., 2014. EosFit7c and a Fortran module (library) for equation of state calculations. Zeitschrift für Kristallographie 229, 405–419.
Bercovici, D., Karato, S., 2003. Whole-mantle convection and the transition-zone water filter. Nature 425, 39–44.
Berman, R.G., 1998. Internally-consistent thermodynamic data for minerals in the system Na2O–K2O–CaO–MgO–FeO–Fe2O3–Al2O3–SiO2–TiO2–H2O–CO2. Journal of Petrology 29, 445–522.
Bolfan-Casanova, N., Mackwell, S., Keppler, H., Rubie, D.C., 2002. Pressure dependence of H solubility in magnesiowustite up to 25 GPa: implications for the storage of water in the Earth's lower mantle. Geophysical Research Letters 29. http://dx.doi.org/10.1029/2001GL014457.
Bolfan-Casanova, N., Keppler, H., Rubie, D.C., 2003. Water partitioning at 660 km depth and evidence for very low water solubility in magnesium silicate perovskite. Geophysical Research Letters 30. http://dx.doi.org/10.1029/2003GL017182.
Brey, G.P., Bulatov, V., Girnis, A., Harris, J.W., Stachel, T., 2004. Ferropericlase – a lower mantle phase in the upper mantle. Lithos 77, 655–663.
Clog, M., Aubaud, C., Cartigny, P., Dosso, L., 2013. The hydrogen isotopic composition and water content of southern Pacific MORB: a reassessment of the D/H ratio of the depleted mantle reservoir. Earth and Planetary Science Letters 381, 156–165.
Emry, E.L., Nyblade, A.A., Julia, J., Anandakrshnan, S., Aster, R.C., Wiens, D.A., Huerta, A.D., Wilson, T.J., 2015. The mantle transition zone beneath West Antarctica: seismic

evidence for hydration and thermal upwellings. Geochemistry, Geophysics, Geosystems 16, 40–58. http://dx.doi.org/10.1002/2014GC005588.
Fei, Y., Mao, H.K., 1993. Static compression of Mg(OH)2 to 78 GPa at high temperature and constraints on the equation of state of fluid H2O. Journal of Geophysical Research 98, 11875–11884.
Frost, D.J., Asahara, Y., Rubie, D.C., Miyajima, N., Dubrovinsky, L.S., Holzapfel, C., Ohtani, E., Miyahara, M., Sakai, T., 2010. Partitioning of oxygen between the Earth's mantle and core. Journal of Geophysical Research 115. http://dx.doi.org/10.1029/2009JB006302.
Gonzalez-Platas, J., Alvaro, M., Nestola, F., Angel, R.J., 2016. EosFit7-GUI: a new GUI tool for equation of state calculations, analyses, and teaching. Journal of Applied Crystallography 49. http://dx.doi.org/10.1107/S1600576716008050.
Goss, J.P., Briddon, P.R., Hill, V., Rayson, M.J., 2014. Identification of the structure of the 3107 cm-1 H-related defect in diamond. Journal of Condensed Matter 26, 14801.
Harte, B., 2010. Diamond formation in the deep mantle: the record of mineral inclusions and their distribution in relation to mantle dehydration zones. Mineralogical Magazine 74, 189–215.
Harte, B., Harris, J.W., 1994. Lower mantle mineral associations preserved in diamonds. Mineralogical Magazine A58, 384–385.
Hernandez, E.R., Alfe, D., Brodholt, J., 2013. The incorporation of water into lower mantle perovskites: a first-principles study. Earth and Planetary Science Letters 364, 37–43.
Hirschmann, M.M., 2006. Water, melting and the deep earth H2O cycle. Annual Review of Earth and Planetary Sciences 34, 629–653.
Hutchinson, M.T., Cartigny, P., Harris, J.W., 1999. Carbon and nitrogen compositions and physical characteristics of transition zone and lower mantle diamonds from São Luiz, Brazil. In: Gurney, J.J., et al. (Eds.), Proceeding of the 7th International Kimberlite Conference. Red Roof Design, Cape Town, pp. 372–382.
Inoue, T., Wada, T., Sasaki, R., Yurimoto, H., 2010. Water partitioning in the Earth's mantle. Physics of the Earth and Planetary Interiors 183, 245–251.
Joachim, B., Wohlers, A., Norberg, N., Gardes, E., Petrishcheva, E., Abart, R., 2013. Diffusion and solubility of hydrogen and water in periclase. Physics and Chemistry of Minerals 40, 19–27.
Kaminsky, F.V., Zakharchenko, O.D., Davies, R., Griffin, W.L., Khachatryan-Blinova, G.K., Shiryaev, A.A., 2001. Superdeep diamonds from Juina area, Mato Grosso State, Brazil. Contributions to Mineralogy and Petrology 140, 734–753.
Kaminsky, F.W., Wirth, R., Schreiber, A., 2014. A microinclusion of lower-mantle rock and other minerals and nitrogen lower-mantle inclusions in a diamond. The Canadian Mineralogist 53, 83–104.
Levy, D., Diella, V., Dapiaggi, M., Sani, A., Gemmi, M., Pavese, A., 2004. Equation of state, structural behaviour and phase diagram of synthetic $MgFe_2O_4$, as a function of pressure and temperature. Physics and Chemistry of Minerals 31, 122–129.
Libowitzky, E., Rossman, G.R., 1996. Principles of quantitative absorbance measurements in anisotropic crystals. Physics and Chemistry of Minerals 23, 319–327.
Libowitzky, E., Rossman, G.R., 1997. An IR absorption calibration for water in minerals. American Mineralogist 82, 1111–1115.
McCammon, C.A., Peyronneau, J., Poirier, J.P., 1998. Low ferric iron content of (Mg,Fe)O at high pressures and temperatures. Geophysical Research Letters 25, 1589–1592.
Nestola, F., Smyth, J.R., 2015. Diamonds and water in the deep Earth: a new scenario. International Geology Review 58 (3), 263–276.
Nimis, P., Alvaro, M., Nestola, F., Angel, R.J., Marquardt, K., Rustioni, G., Harris, J.W., 2016. First evidence of hydrous silicic fluid films around solid inclusions in gem-quality diamonds. Lithos 260, 384–389.
Ohtani, E., Litasov, K., Hosoya, T., Kubo, T., Kondo, T., 2004. Water transport into the deep mantle and formation of a hydrous transition zone. Physics of the Earth and Planetary Interiors 143-144, 255–269.
Palot, M., Cartigny, P., Harris, J.W., Kaminsky, F.V., Stachel, T., 2012. Evidence for deep mantle convection and primordial heterogeneity from nitrogen and carbon stable isotopes in diamond. Earth and Planetary Science Letters 357-358, 179–193.
Panero, W.R., Pigott, J.S., Reaman, D.M., Kabbes, J.E., Liu, Z., 2015. Dry (Mg,Fe)SiO_3 perovskite in the Earth's lower mantle. Journal of Geophysical Research 120, 894–908.
Pearson, D.G., Brenker, F.E., Nestola, F., McNeill, J., Nasdala, L., Hutchison, M.T., Matveev, S., Mather, K., Silversmit, G., Schmitz, S., Vekemans, B., Vincze, L., 2014. Hydrous mantle transition zone indicated by ringwoodite included within diamond. Nature 507, 221–224.
Prescher, C., McCammon, C., Dubrovinsky, L., 2012. MossA – a program for analyzing energy –domain Mossbauer spectra from conventional and synchrotron sources. Journal of Applied Crystallography 45, 329–331.
Rohrbach, A., Schmidt, M.W., 2011. Redox freezing and melting in the Earth's deep mantle resulting from carbon–iron redox coupling. Nature 472, 209–212.
Schmandt, B., Jacobsen, S.D., Becker, T.W., Liu, Z., Dueker, K.G., 2014. Dehydration melting at the top of the lower mantle. Science 344, 1265.
Smyth, J.R., 1987. β-Mg2SiO4: a potential host for water in the mantle? American Mineralogist 72, 1051–1055.
Stachel, T., Harris, J.W., Aulbach, S., Deines, P., 2002. Kankan diamonds (Guinea) III: $\delta^{13}C$ and nitrogen characteristics of deep diamonds. Contributions to Mineralogy and Petrology 142, 465–475.
Thomson, A.R., Walter, M.J., Kohn, S.C., Brooker, R.A., 2016. Slab melting as a barrier to deep carbon subduction. Nature 529, 76–79.
Walter, M.J., Kohn, S.C., Araujo, D., Bulanova, G.P., Smith, C.B., Gaillou, E., Wang, J., Steele, A., Shirey, S.B., 2011. Deep mantle cycling of oceanic crust: evidence from diamonds and their mineral inclusions. Science 334, 54–57.
Wang, X.C., Wilde, S.A., Li, Q.L., Yang, Y.N., 2015. Continental flood basalts derived from the hydrous mantle transition zone. Nature Communication http://dx.doi.org/10.1038/ncomms8700.
Wirth, R., Dobrzhinetskaya, L., Harte, B., Schreiber, A., Green, H.W., 2014. High-Fe (Mg, Fe)O inclusion in diamond apparently from the lowermost mantle. Earth and Planetary Science Letters 404, 365–375.